ELSEVIER

Available online at www.sciencedirect.com

SciVerse ScienceDirect

Ceramics International 39 (2013) 3129–3134

CERAMICS INTERNATIONAL

www.elsevier.com/locate/ceramint

Photocatalytic activity under visible light of Fe-doped CeO_2 nanoparticles synthesized by flame spray pyrolysis

D. Channei[a,d], B. Inceesungvorn[a], N. Wetchakun[b], S. Phanichphant[c,*], A. Nakaruk[d,*], P. Koshy[d], C.C. Sorrell[d]

[a]*Department of Chemistry, Faculty of Science, Chiang Mai University, Chiang Mai 50200, Thailand*
[b]*Department of Physics and Materials Science, Faculty of Science, Chiang Mai University, Chiang Mai 50200, Thailand*
[c]*Materials Science Research Center, Faculty of Science, Chiang Mai University, Chiang Mai 50200, Thailand*
[d]*School of Materials Science and Engineering, University of New South Wales, Sydney, NSW 2052, Australia*

Received 8 August 2012; received in revised form 26 September 2012; accepted 27 September 2012
Available online 3 October 2012

Abstract

CeO_2 nanoparticles (undoped and Fe-doped) were synthesised using flame spray pyrolysis with varying Fe-dopant concentrations. X-ray diffraction analysis revealed the absence of any impurity phases in all samples. BET (Brunauer, Emmett and Teller) tests showed that the average sizes of undoped and Fe-doped CeO_2 particles were 6.39 and 5.94 nm, respectively. Specific surface area of the particles increased with increasing Fe-dopant concentration. High resolution transmission electron microscopy (HRTEM) revealed that the nanoparticles were either spherical or equiaxed in shape. UV–vis spectroscopy showed a shift of the adsorption edge towards longer wavelengths along with a decrease in the optical indirect band gap from 3.18 to 2.90 eV for undoped particles and 2 mol% Fe-doped particles. In terms of photocatalytic performance, Fe-doped CeO_2 nanoparticles were responsible for an increased degradation of the carbon from formic and oxalic acids. Furthermore, the photocatalytic efficiency was ~100% when 2 mol% Fe-doped CeO_2 particles were used for testing.

Keywords: D. CeO_2; Nanoparticles; Flame Spray Pyrolysis; Photocatalytic Activity

1. Introduction

There have been an increasing experimental focus on characterising cerium dioxide (ceria, CeO_2) which has been identified to possess a unique photocatalytic activity, in addition to high chemical stability, and low biological toxicity. CeO_2 has been used for a wide range of applications, including solar cells, for water purification [1], gas sensors [2,3], and as polishing agents [4]. Furthermore, compared to other metal oxides such as TiO_2, ZnO, and Al_2O_3, CeO_2 has no deleterious effect on human cells [5,6], and therefore use of ceria for photocatalytic applications such as water purification and food packaging will pose minimal risk for humans. On the other hand, ceria is slightly more expensive, and it is also hygroscopic in nature.

CeO_2 is a large band gap semiconductor with an optical indirect band gap of 3.20 eV [7], which limits its application to within the ultraviolet (UV) radiation range. In order to reduce the band gap and to enhance the photoactivity of CeO_2, transition metals ions of variable valency have been introduced into the CeO_2 lattice viz., iron (Fe) [8], copper (Cu) [9], nickel (Ni) [10], manganese (Mn) [11], cobalt (Co) [12] and silver (Ag) [13]. Of these ions, iron is considered to be one of the most promising candidate, since Fe^{3+} can easily substitute for Ce-ions or enter the interstices of the crystal lattice of CeO_2 [14], leading to the creation of donor or accepter levels between the valence and conduction bands [15].

Several techniques have been used to prepare CeO_2 nanoparticles, including hydrothermal synthesis [16], homogeneous precipitation [17], sonochemical synthesis

---

*Corresponding authors.
E-mail addresses: sphanichphant@yahoo.com (S. Phanichphant), a.nakaruk@unsw.edu.au (A. Nakaruk).

0272-8842/$ - see front matter © 2012 Elsevier Ltd and Techna Group S.r.l. All rights reserved.
http://dx.doi.org/10.1016/j.ceramint.2012.09.093

[18], and flame spray pyrolysis (FSP) [19]. The latter is an attractive, versatile, and practical method to prepare CeO_2 nanoparticles due to several advantages such as low cost, simplicity of operation and experimental setup, capacity for mass production, ease of doping, reproducibility, and rapid particle growth.

Thus, it is clear that the preparation and use of CeO_2 nanopaticles doped with Fe by flame spray pyrolysis would be advantageous; moreover, there is a potential for improving the photocatalytic performance of the material. Therefore, the present work aims: (1) to synthesise CeO_2 nanoparticles doped with Fe using flame spray pyrolysis, and (2) to analyse these particles in terms of their mineralogical and morphological characteristics, and photocatalytic performance.

2. Experimental procedure

2.1. Synthesis of CeO_2 nanoparticles

Cerium nitrate-hexahydrate ($Ce(NO_3)_3 \cdot 6H_2O$, Sigma-Aldrich, 99.99%) and iron acetyl-acetonate ($Fe(C_5H_7O_2)_3$, Sigma-Aldrich, 97%) were used as the sources of cerium and iron, respectively. The precursors were prepared by dissolving cerium nitrate-hexahydrate in ethanol solution (Scharlau, 99.9%) at 0.5 M Ce concentration. The Fe-dopant concentrations used were 0.25, 0.50, 0.75, 1.00, 1.50, and 2.00 mol%. During the synthesis process, the precursor was fed into a FSP reactor using a syringe pump at a feed rate of 5 mL/min and the dispersion rate of O_2 was fixed at 5 L/min. The flow rates of combustion gases were fixed at 1.19 and 2.46 L/min for methane and O_2, respectively. The pressure at the nozzle tip was set at 1.5 bars. Finally, the synthesised nanoparticles were collected on a glass microfiber with the aid of a vacuum pump.

2.2. Characterisation

The mineralogy of the nanoparticles was analysed using X-ray diffraction (XRD; Philips X'pert MPD; CuKα radiation; 45 kV; 40 mA; step size 0.02° 2θ; scanning speed 5.5° 2θ/min; aluminium sample holder). The mean particle size and specific surface area (SSA) were evaluated using the Brunauer, Emmett, and Teller (BET) nitrogen adsorption method (Quantachrome *Autosorp 1 MP*; 0.25 g sample; 1 h at 150 °C degassing). High resolution transmission electron microscopy (HRTEM, JEOL *JEM-2010*; 200 kV accelerating voltage) was used to determine the particle size distribution and particle morphology of the synthesised particles. The amount of dopant present in the synthesised particles was confirmed using energy-dispersive X-ray spectroscopy (EDS; JEOL *JSM-6335F*; 15 kV accelerating voltage). The reflectance of nanoparticles (mounted in the recess of a standard aluminium sample support) was obtained using a UV–vis spectrophotometer equipped with an integrating sphere detector (Perkin Elmer *Lambda 950*, 300–800 nm, monochromatic, 400 nm/min, step size 1 nm). The absorbance spectra were used to calculate the optical indirect band gap using the Schuster–Kubelka–Munk equation [20,21].

2.3. Photocatalytic activity

The photocatalytic performances of nanoparticles were assessed in terms of the decomposition of both formic acid (HCOOH) and oxalic acid $(COOH)_2$ in a spiral reactor under UV irradiation from a fluorescent lamp (Sylvania fluorescent lamp, 18 W) filtered with a Rosco® E-colour UV filter, as shown in Fig. 1. The radiation was filtered using a double layer of UV cut-off filter (Rosco E-Colour, 360–400 nm).

The spiral reactor conduit included a borosilicate glass tube of dimensions 5 mm OD and 3 mm ID, which was formed into a coil of 50 mm OD and 700 mm length. The light source (30 mm diameter, 700 mm length) was centred within the coil. This assembly was wrapped with an outer layer of aluminium foil as a light shield. The solution was circulated continuously through the conduit using a peristaltic pump (Masterflex Model 7553-79; 7.0 mL/min) with silicone tubing. These conditions resulted in an operating temperature of the recirculating solution of ~28 °C.

Nanoparticles were suspended in a solution of 50 mL ethanol, and then dispersed into a vibra-cell sonicator (Sonics *VCX 750*) for 20 min. The suspension then was loaded into a spiral photoreactor. Oxalic acid or formic acid equivalent to 500 μg carbon was injected into the photocatalytic suspension through the inlet port. The photocatalytic efficiency was determined based on the carbon dioxide (CO_2) generation rate using a conductivity metre (Eutech Instrument *Cyberscan PC 5500/5000*). The overall organic compound degradation process can be summarised in terms following equations [22]:

$$\text{Oxalic acid}: \quad (COOH)_2 + 2OH\cdot \longrightarrow 2CO_2 + 2H_2O \qquad (1)$$

$$\text{Formic acid}: \quad HCOOH + 2OH\cdot \longrightarrow CO_2 + 2H_2O \qquad (2)$$

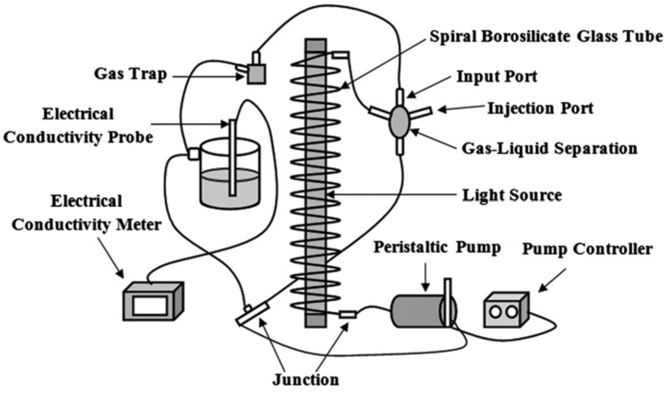

Fig. 1. Schematic of the photocatalytic activity test system.

3. Results and discussion

The XRD patterns shown in Fig. 2 indicate that cerium dioxide with cubic fluorite structure is the only crystalline phase present in both undoped and Fe-doped CeO_2 nanoparticle samples. Potential impurity phases such as Fe_2O_3, $FeCeO_3$, and $FeCe_2O_4$ were not observed. Moreover, the peak intensity of (111) plane was seen to decrease with increasing Fe-dopant concentration. This implies that the increasing incorporation of Fe ions into the CeO_2 lattice tends to lower the crystallinity of the latter due to introduction of anharmonicities in the lattice by the foreign cation. The crystallite sizes of the nanoparticles were determined using Scherrer's equation [23] and the values are presented in Table 1. From the table, it is seen that the crystallite sizes decreased with increasing Fe-dopant concentrations.

The increase in the dopant concentration was observed to lower the crystallite size in addition to decreasing the crystallinity of the nanoparticles (as seen from the decreasing crystallite sizes in Table 1). Moreover, it can be noted that doping CeO_2 with Fe^{3+} can hinder the grain growth as well, and this supports the observance of decreasing crystallite sizes [24,25].

The specific surface area (SSA) of CeO_2 nanoparticles was found to increase with increasing Fe-dopant concentrations as shown in both Fig. 3 and Table 1. This supports the data on the crystallite sizes of the nanoparticles such that seen that small particle sizes have greater surface areas.

The BET equivalent particle size was determined using the following equation [26]:

$$d_{\mathrm{BET}} = \frac{6}{\rho_{\mathrm{CeO_2}} \times \mathrm{SSA}} \tag{3}$$

where d_{BET} is the mean BET diameter, $\rho_{\mathrm{CeO_2}}$ is the bulk density of CeO_2 ($\approx 7.215\ \mathrm{g/cm^3}$) [27] and SSA is the Specific surface area

The particle size of CeO_2 is shown in Table 1. In general, the crystallite size is not equal to the actual particle size due to agglomeration effects in the latter [28]. However, these results show that particle sizes are very close in value to the crystallite sizes; and this clearly indicates that the particles synthesised are single crystals [29].

Fig. 4 shows the high resolution transmission electron microscopy (HRTEM) images of Fe-doped CeO_2. The images clearly demonstrate that undoped and Fe-doped CeO_2 nanoparticles are spherical or equiaxed in shape. The distribution of particle diameters calculated from HRTEM micrographs has been found to be in the range of 6.25–10 nm for undoped CeO_2 and 5.00–6.25 nm for 2 mol% Fe-doped CeO_2. These results support the crystallite size measurements and BET results which showed that increasing Fe-dopant concentrations result in a lowering of the particle sizes of CeO_2.

Semi-quantitative elemental analysis of the Ce, O, and Fe concentrations were carried out using energy dispersive

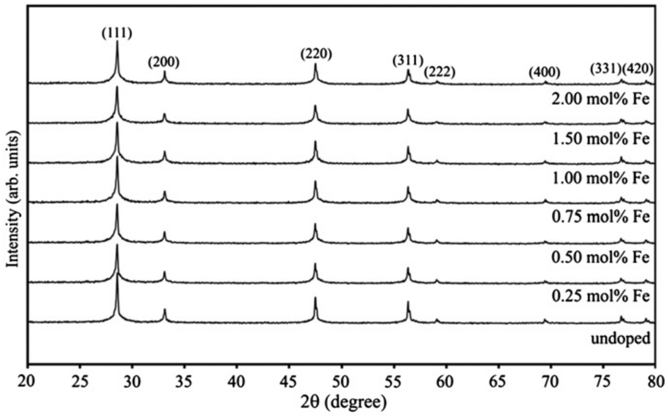

Fig. 2. X-ray diffraction (XRD) patterns of CeO_2 nanoparticles as a function of dopant concentration.

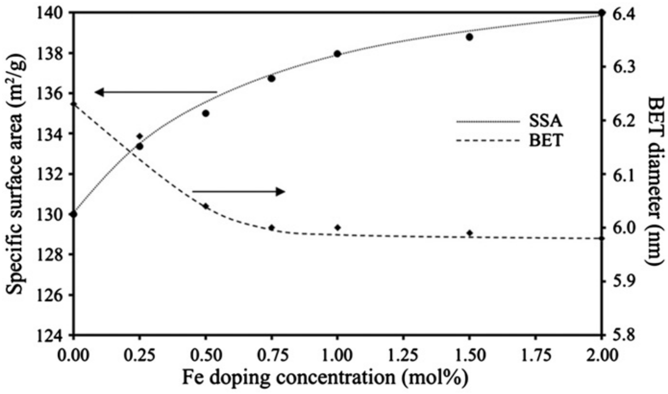

Fig. 3. Variation in the specific surface area (SSA) and BET particle size of CeO_2 nanoparticles as a function of the dopant concentration.

Table 1
Summary of analytical data.

Parameters	**Dopant concentration (mol% Fe)**						
	0.00	**0.25**	**0.50**	**0.75**	**1.00**	**1.50**	**2.00**
Crystallite size (nm)	7.15	6.70	6.65	6.60	6.41	6.31	6.22
Particle size (BET diameter, nm)	6.39	6.23	6.16	6.08	6.02	5.99	5.94
Particle size (TEM, nm)	6.25–10.00	7.50–9.50	6.50–9.00	6.50–9.00	5.00–6.25	5.00–6.25	5.00–6.25
Specific surface area (SSA, m^2/g)	130.00	133.38	135.00	136.73	137.97	138.80	140.00
Fe concentration(at%)	0.00	0.19	0.36	0.63	0.96	1.38	1.73
Energy band gap (eV)	3.18	3.13	3.10	3.06	3.00	2.98	2.90

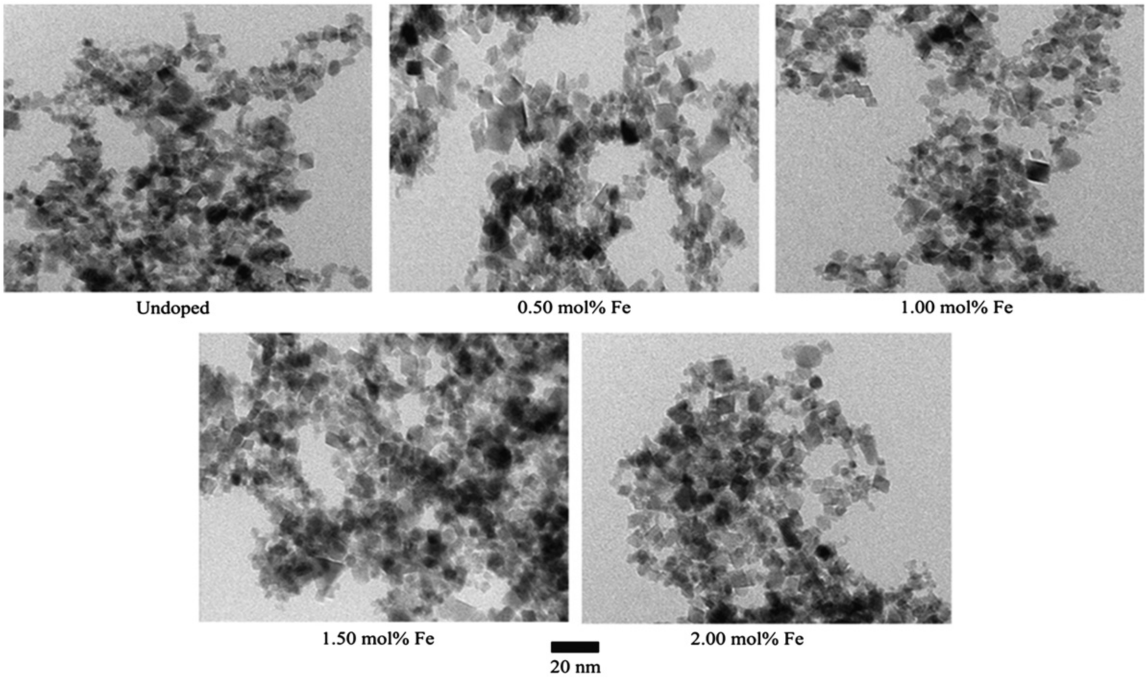
Undoped

0.50 mol% Fe

1.00 mol% Fe

1.50 mol% Fe

2.00 mol% Fe

Fig. 4. High resolution transmission electron microscopy (HRTEM) images of CeO_2 nanoparticles synthesised at varying dopant concentrations.

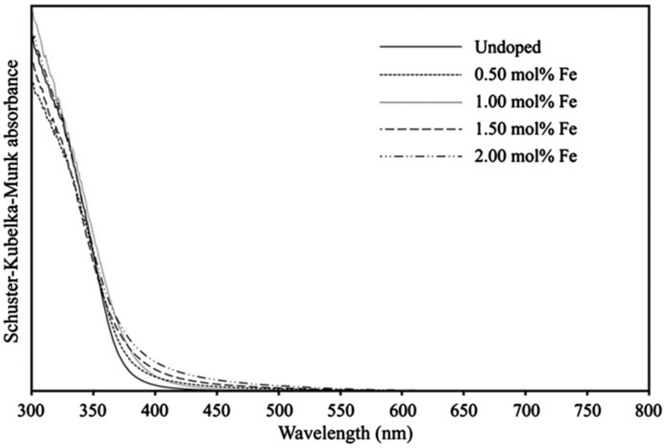

Fig. 5. Schuster–Kubelka–Munk absorbance plot of CeO_2 nanoparticles as a function of dopant concentration.

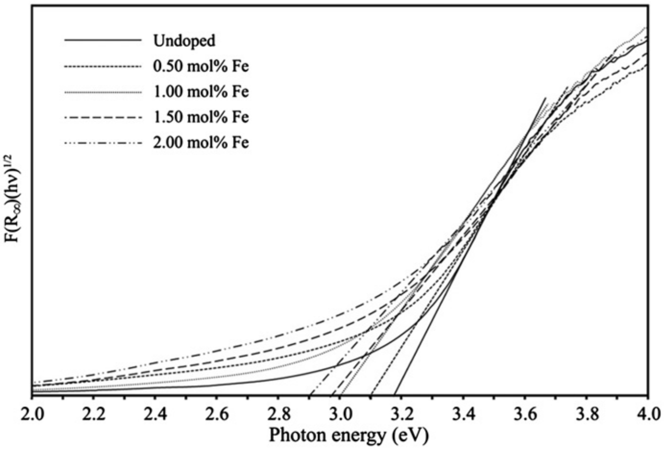

Fig. 6. Optical indirect band gaps of CeO_2 nanoparticles as a function of dopant concentrations.

spectrometry (EDS). As seen in Table 1, the composition of the dopant in the sample was close to the dopant concentration of the starting material. This clearly shows that Fe ions have entered the CeO_2 lattice either interstitially or substitutionally.

The Schuster–Kubelka–Munk absorbance data were calculated from UV–vis reflection data using the following equation [20,21]

$$\frac{F(R_\infty)=(1-R_\infty)^2}{2R_\infty} \qquad (4)$$

where $F(R_\infty)$ is proportional to the absorption constant of the material at a particular wavelength R_∞ is the reflectance of the sample (%)

The plot of $F(R_\infty)$ vs. wavelength of CeO_2 nanoparticles is shown in Fig. 5. The spectra show that the adsorption edge shifted towards longer wavelengths (red-shift) with increasing Fe-dopant concentration. Fig. 6 shows the optical indirect band gaps of CeO_2 nanoparticles, and this figure suggests that an increase in the dopant concentration results in a lowering of the optical indirect band gap. The lowest band gap value is seen in the case of the 2.00 mol% Fe-doped CeO_2 nanoparticles.

The reason for the enhanced performance in the case of doped CeO_2 is due to the fact that the addition of Fe ions results in the formation of interstitial sites which in turn create new energy levels (impurity energy levels) between the valence and conduction bands [30]. The impurity energy levels allow for intrinsic band gap excitation under

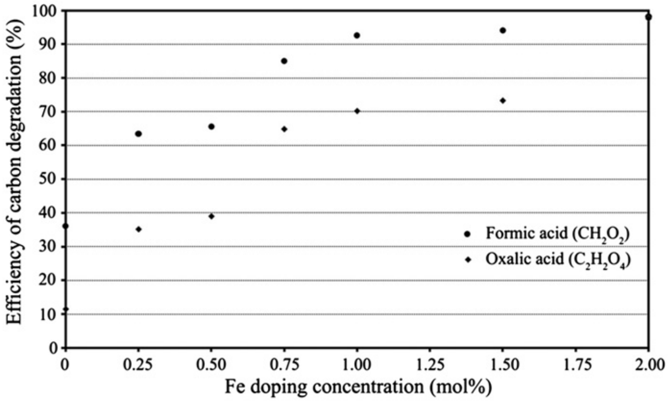

Fig. 7. Variation in the efficiency of formic and oxalic acid degradation by CeO_2 nanoparticles at varying dopant concentrations.

visible light region, and this implies that the higher energy state of 3d-electrons from Fe-cation dopants can be excited to the conduction band of CeO_2 [31], thereby enhancing its photocatalytic performance.

The photocatalytic efficiency of CeO_2 nanoparticles was calculated by measuring the CO_2 gas formed as a by-product of formic or oxalic acid degradation. Fig. 7 shows the variation in the efficiency of CeO_2 nanoparticles as a function of the dopant concentration. From this figure, it is clearly seen that the efficiency of degradation of carbon is enhanced at increasing Fe-dopant concentrations.

Comparing the formulae for formic acid (HCOOH) and oxalic acid $(COOH)_2$, it is seen that the efficiency of carbon degradation in formic acid is greater than the case for oxalic acid at low Fe-dopant concentrations. However, at 2 mol% Fe, the efficiencies of acid degradation were similar i.e. $\sim$100% for both acids. The reasons for this are due to the following: (1) the defects on the catalyst surface formed during synthesis can trap and prevent electron–hole recombination [32], thereby lowering recombination rates, (2) the increase in surface area can provide more sites for adsorption of organic atoms on the surface of the CeO_2 particles, and (3) decreasing optical indirect band gaps can enhance the light absorption of CeO_2 nanoparticles, and thereby enhance the photocatalytic performance leading to the degradation of organics.

4. Conclusions

The present work has successfully synthesised Fe-doped CeO_2 nanoparticles using the flame spray pyrolysis method. The CeO_2 nanoparticles produced were of cubic fluorite structure with no impurity phases present. The BET results showed that the CeO_2 particles sizes decreased from 6.39 nm (undoped) to 5.94 nm (2.00 mol% Fe-dopant). Moreover, the SSA increased with increasing Fe-dopant concentration. HRTEM analysis revealed that the nanoparticles were either spherical or equiaxed in appearance.

The shifting of the absorption edge in visible region towards longer wavelengths was found in the case of Fe-doped CeO_2 nanoparticles, and this lowered the optical indirect band gap of CeO_2 nanoparticles from 3.18 eV (undoped) to 2.90 eV (2.00 mol% Fe-dopant). Under visible light irradiation, the efficiency of formic and oxalic acid degradations by Fe-doped CeO_2 nanoparticles was superior to that of undoped nanoparticles. Furthermore, the photocatalytic performance of 2 mol% Fe-doped CeO_2 nanoparticles resulted in almost complete degradation of both formic and oxalic acids.

Acknowledgements

The authors are grateful for the financial support provided through the Royal Golden Jubilee Scholarship Project of Thailand, which has allowed this work to be undertaken. The authors also wish to thank Dr. Pat Photongkum (School of Materials Science and Engineering, UNSW) for assistance in obtaining data for optical band gap and UV–vis spectrophotometry and Dr. Chawarat Siriwong (Silpakorn University, Thailand) for assistance in nanoparticle preparation.

References

[1] P.I. Ji, J. Zhang, F. Chen, M. Anpo, Study of adsorption and degradation of acid orange on the surface of CeO_2 under visible light irradiation, Applied Catalysis B 85 (2009) 148–154.

[2] N. Izu, W. Shin, N. Murayama, S. Kanzaki, Resistive oxygen gas sensors based on CeO_2 fine powder prepared using mist pyrolysis, Sensors and Actuators B 87 (2002) 95–98.

[3] D.W. Lee, J.W. Lee, T.S. Jang, B.K. Kim, Oxygen sensitivity of nanostructured cerium oxide prepared by a thermochemical process, Journal of Ceramic Processing Research 7 (2006) 148–151.

[4] V.D. Kosynkin, A.A. Arzgatkina, E.N. Ivanov, M.G. Chtousta, A.I. Grabko, A.V. Kardapolov, N.A. Sysina, The study of process production of polishing powder based on cerium dioxide, Journal of Alloys and Compounds 303–304 (2000) 421–425.

[5] I.S. Kim, M. Beak, S.J. Choi, Comparative cytotoxicity of Al_2O_3, CeO_2, TiO_2 and ZnO nanoparticles to Human lung cells, Journal for Nanoscience and Nanotechnology 10 (2010) 3453–3458.

[6] B. Johnston, T.M. Scown, J. Moger, S.A. Cumberland, M. Baalousha, K. Linge, R. van Aerle, K. Jarvis, J.R. Lead, C.R. Tyler, Bioavailability of nanoscale metal oxides TiO_2, CeO_2, and ZnO to fish, Environmental Science and Technology 44 (44) (2010) 1144–1151.

[7] P.J. Hay, R.L. Martin, J. Uddin, G.E. Scuseria, Theoretical study of CeO_2 and Ce_2O_3 using a screened hybrid density functional, Journal of Chemical Physics 25 (2006) article no. 034712.

[8] W.Q. Ye, Z.H. Wu, Y.Q. Hui, L. Sheng, X.D. Gang, Y.J. Quan, Fe doped polycrystalline CeO_2 as terahertz optical material, Chinese Physics Letters 26 (2009) article no. 047803.

[9] L.S. Neiva, E. Leal, A.C.F. Melo Costa, A.J.S. Mascarenhas, H.M.C. Andrade, L. Gama, Evaluation of the Cu doping effects in CeO_2 catalytic supports obtained by combustion reaction, Materials Science Forum 660–661 (2010) 899–903.

[10] S. Kumar, Y.J. Kim, B.H. Koo, C.G. Lee, Structural and magnetic properties of Ni loaded CeO_2 nanoparticles, Journal for Nanoscience and Nanotechnology 10 (2010) 7204–7207.

[11] E.L. Santos, R. Muccillo, E.N.S. Muccillo, Densification and electrical conductivity of Mn-doped CeO_2, Materials Science Forum 591–593 (2008) 639–643.

[12] S. Kumar, Y.J. Kim, B.H. Koo, H. Choi, C.G. Lee, Structural and magnetic properties of Co doped CeO_2 nano-particles, IEEE Transactions on Magnetics 45 (2009) 2439–2441.

[13] C. Kitiwiang, S. Phanichphant, Synthesis of silver-doped cerium dioxide nanoparticles by the homogeneous precipitation, Journal of the Microscopy Society of Thailand 23 (2009) 83–86.

[14] C. Liang, Z. Ma, H. Lin, L. Ding, J. Qiu, W. Frandsen, D. Su, Template preparation of nanoscale $Ce_xFe_{1-x}O_2$ solid solutions and their catalytic properties for ethanol steam reforming, Journal of Materials Chemistry 19 (2009) 1417–1424.

[15] Z. Wang, Z. Quan, J. Lin, Remarkable changes in the optical properties of CeO_2 nanocrystals induced by lanthanide ions doping, Inorganic Chemistry 43 (2007) 5237–5242.

[16] T. Masui, H. Hirai, N. Imanaka, Synthesis of cerium oxide nanoparticles by hydrothermal crystallization with citric acid, Journal of Materials Science Letters 21 (2004) 489–491.

[17] H.I. Chen, H.Y. Chang, Homogeneous precipitation of cerium dioxide nanoparticles in alcohol/water mixed solvents, Colloids and Surfaces A 242 (2004) 61–69.

[18] L.X. Yin, Y.Q. Wang, G.S. Pang, Y. Koltypin, A. Gedanken, Sonochemical synthesis of cerium oxide nanoparticles—effect of additives and quantum size effect, Journal of Colloid and Interface Science 246 (2002) 78–84.

[19] A. Gojova, J.T. Lee, H.S. Jung, B. Guo, A.I. Barakat, I.M. Kennedy, Effect of cerium oxide nanoparticles on inflammation in vascular endothelial cells, Inhalation Toxicology 21 (2009) 123–130.

[20] K. Chiang, R. Amal, T. Tran, Photocatalytic degradation of cyanide using titanium dioxide modified with copper oxide, Advances in Environmental Research 6 (2002) 471–485.

[21] J. Sirita, S. Phanichphant S, F.C. Meunier, Quantitative analysis of adsorbate concentrations by diffuse reflectance FTIR, Analytical Chemistry 79 (2007) 3912–3918.

[22] J. Krýsa, L. Vodehnal, J. Jirkovský, Photocatalytic degradation of oxalic acid on a semiconductive layer of n-TiO_2 particles in a batch mode plate photoreactor part II: light intensity limit, Journal of Applied Electrochemistry 29 (1999) 429–435.

[23] A.L. Patterson, The scherrer formula for X-ray particle size determination, Physical Review 56 (1939) 978–982.

[24] A. Azam, A.S. Ahmed, M. Chaman, A.H. Naqvi, Investigation of electrical properties of Mn doped tin oxide nanoparticles using impedance spectroscopy, Journal of Applied Physics 108 (2010) article no. 094329.

[25] Z.M. Tiana, S.L. Yuan, J.H. Hea, P. Lia, S.Q. Zhanga, C.H. Wanga, Y.Q. Wanga, S.Y. Yina, L. Liu, Structure and magnetic properties in Mn doped SnO_2 nanoparticles synthesized by chemical co-precipitation method, Journal of Alloys and Compounds 466 (2008) 26–30.

[26] S. Brunauer, P.H. Emmett, E. Teller, Adsorption of gases in multimolecular layers, Journal of the American Chemical Society 60 (1938) 309–319.

[27] N. Wetchakun, S. Phanichphant, Synthesis and characterization of novel ZnS/CeO_2 nanocomposites, in: Micro Engineered and Molecular Systems (NEMS), 5th IEEE International Conference, 2010, pp. 93–37.

[28] T. Itoh, Particle and crystallite sizes of ZrO_2 powder obtained by the calcination of hydrous zirconia, Journal of Materials Science Letters 4 (1985) 431–433.

[29] D. Lewis, D.O. Northwood, Evaluation of crystallite size and microstrains in cold-worked lithium fluoride from X-ray diffraction line profile, Journal of Physics D 2 (1969) 21–26.

[30] G.F. Zhang, G. Fang, L.L. Ping, G.S. Li, X.Q. Qiu, Hydrothermal synthesis and characterization of $Ce_{1-x}Mn_xO_{2-\delta}$ solid solutions, Chinese Journal of Structural Chemistry 29 (2010) 307–313.

[31] M. Al Khana, S.I. Woo, O.B. Yang, Hydrothermally stabilized Fe (III) doped titania active under visible light for water splitting, International Journal of Hydrogen Energy 33 (2008) 5345–5351.

[32] C.L. Luu, Q.T. Nguyen, S.T. Ho, Synthesis and characterization of Fe-doped TiO_2 photocatalyst by the sol–gel method, Advances in Natural Science 1 (2010) 1–5.